BOLETIN DE LA SOCIEDAD ESPAÑOLA DE
Cerámica y Vidrio
www.elsevier.es/bsecv

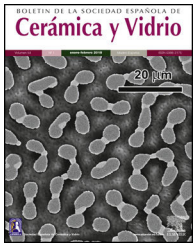

Effect of the pH pre-adjustment on the formation of $In_2W_3O_{12}$ and In_6WO_{12} powders: Cluster coordination and optical band gap

Rafael Texeira de Paiva[a], *Içamira Costa Nogueira*[b], *Júlio César Sczancoski*[c], *Pablo Santana Lemos*[c], *José Milton Elias Matos*[a], *Reginaldo Silva Santos*[e], *Elson Longo*[d], *Laécio Santos Cavalcante*[a,e,*]

[a] *Programa de Pós-Graduação em Ciência dos Materiais-PPCM, Universidade Federal do Piauí, Teresina, PI 64049-550, Brazil*
[b] *ICE-Universidade Federal do Amazonas, Av. Rodrigo Otávio Japiim, P.O. Box 670, 69077-000 Manaus, AM, Brazil*
[c] *DQ-UFSCar, Universidade Federal de São Carlos, P.O. Box 676, São Carlos, SP 13565-905, Brazil*
[d] *Departamento de Físico-Química, Universidade Estadual Paulista, 14800-060 Araraquara, SP, Brazil*
[e] *PPGQ-GERATEC, Universidade Estadual do Piauí, Rua: João Cabral, N. 2231, P.O. Box 381, 64002-150 Teresina, PI, Brazil*

ARTICLE INFO

Article history:
Received 8 November 2018
Accepted 20 February 2019
Available online 23 April 2019

Keywords:
$In_2W_3O_{12}$
In_6WO_{12}
Rietveld refinement
Clusters
Optical band gap

ABSTRACT

In this communication, diindium tristungstate ($In_2W_3O_{12}$) and hexaindium tungstate (In_6WO_{12}) powders were synthesized by the co-precipitation method at different pH values and heat treatment at 1073 K for 2 h. X-ray diffraction patterns and Rietveld refinements were employed to analyze the long-range structural ordering as well as quantify the presence crystallographic phases, respectively. All powders obtained in pH ranging from 2 to 3.5 exhibited a mixture of $In_2W_3O_{12}$ and gamma-tungsten oxide (γ-WO_3) phases. When prepared at pH close to 4, the powders presented both $In_2W_3O_{12}$ and In_6WO_{12} phases. All these crystalline structures were simulated in a three-dimensional visualization program by adopting the Rietveld refinements analysis as input data. The ultraviolet–visible spectra were employed to estimate the optical band gap energy of all powders for the first time.

Efecto del preajuste de pH en la formación de polvos $In_2W_3O_{12}$ e In_6WO_{12}: coordinación de grupo y banda óptica

Palabras clave:
$In_2W_3O_{12}$
In_6WO_{12}
Refinamiento Rietveld
Clústers
Brecha de banda óptica

RESUMEN

En esta comunicación, los polvos tristungstate de diindio ($In_2W_3O_{12}$) y tungstato de hexaindio (In_6WO_{12}) se sintetizaron mediante el método de co-precipitación a diferentes valores de pH y tratamiento térmico a 1.073 K durante 2 h. Se emplearon patrones de difracción de rayos X y refinamientos de Rietveld para analizar el ordenamiento estructural de largo alcance y cuantificar las fases cristalográficas de presencia, respectivamente. Todos los polvos obtenidos en un pH de 2 a 3,5 mostraron una mezcla de fases $In_2W_3O_{12}$ y óxido de tungsteno gamma (γ-WO_3). Cuando se prepararon a un pH cercano a 4, los polvos

* *Corresponding author.*
E-mail address: laeciosc@gmail.com (L.S. Cavalcante).
https://doi.org/10.1016/j.bsecv.2019.02.001

presentaron las fases $In_2W_3O_{12}$ e In_6WO_{12}. Todas estas estructuras cristalinas se simularon en un programa de visualización tridimensional mediante la adopción del análisis de refinamiento de Rietveld como datos de entrada. Los espectros ultravioleta-visibles se emplearon para estimar la energía del intervalo de banda óptica de todos los polvos por primera vez.

Introduction

In the last years, trivalent tungstates, as diindium tris-tungstate [$In_2(WO_4)_3$ or $In_2W_3O_{12}$] and hexaindium tungstate (In_6WO_{12}), have been especially synthesized by using *top down* (TD) approaches [1–6]. The TD approach involves the breaking down of bulk materials up to achieve nanometer-size particles. The most popular TD methods employ mixture of precursor powders, repeated attrition or milling cycles, and heat treatments performed at high temperatures for long reaction times [7–11]. Despite the simplicity and easy handling, the final products are able to present large grains, reduced surface area, nonuniform particle shapes and sizes, broad particle size distribution, and a significant amount of impurities [12].

In order to minimize theses drawbacks, a good strategy to prepare crystalline $In_2W_3O_{12}$ or In_6WO_{12} oxides is by means of *bottom-up* (BU) approaches. In BU approach, small building blocks (atomic and/or molecular species) are self-assembled to produced complex nanostructures, but with an efficient control on the particle sizes and shapes (nano-, meso-, or microscale) [13,14]. In general, trivalent tungstates (powder or thin film) have been synthesized by co-precipitation reaction, sol–gel, salt molten, and hydrothermal processing [15–18].

In terms of crystalline structure, $In_2W_3O_{12}$ exhibits an orthorhombic structure with space group (*Pnca*) at room temperature. On the other hand, at approximately 531 K, this tungstate crystallize in a monoclinic structure with space group ($P2_1/a$) [19,20]. A curious feature of $In_2W_3O_{12}$ is that its orthorhombic structure has a negative thermal expansion coefficient for temperatures above 523 K, while the monoclinic structure exhibit a positive thermal expansion coefficient for temperatures lower than 523 K [21].

Different electronic properties of both $In_2W_3O_{12}$ and In_6WO_{12} oxides have been investigated, such as inorganic scintillators [22], luminescence [23], electrochromic [24], *n*-type semiconductor with low conductivity [25], trivalent-cation conductor [26], and photocatalysis [27]. However, in our understanding, the literature yet not reported the optical band gap behavior at room temperature of these kinds of trivalent tungstates.

Therefore, in this short communication, we report on the formation of $In_2W_3O_{12}$ and In_6WO_{12} powders prepared by the co-precipitation method (at 363 K for 1 h) at different pH pre-adjustment values (from 2 to 4). The obtained amorphous precipitates were crystallized by means of heat treatments at 1073 K for 2 h. The structural ordering as well as crystalline phase identification and quantification were investigated in details by X-ray diffraction (XRD) and Rietveld refinement analysis, respectively. The ultraviolet–visible (UV–Vis) spectroscopy was a powerful tool in order to estimate the optical band gap energies of these tungstates.

Experimental details

Synthesis of $In_2W_3O_{12}$ and $In_6W_3O_{12}$ powders

The synthesis of $In_2W_3O_{12}$ and $In_6W_3O_{12}$ powders is described as follows: 3×10^{-3} mol of sodium tungstate (VI) dihydrate ($Na_2WO_4{\cdot}2H_2O$; 99.0% purity, Sigma–Aldrich) and 2×10^{-3} mol of indium (III) nitrate hydrate [$In(NO_3)_3{\cdot}H_2O$; 99.99% purity, Sigma–Aldrich] were separately placed in two plastic tubes (Falcon, capacity of 60 mL) and dissolved with 50 mL of deionized water (DI-H_2O). The first solution, containing, $Na^+_{(aq)}$ and $WO^{2-}_{4(aq)}$ ions, was transferred into a beaker and the volume was completed with 50 mL of DI-H_2O. This same procedure was adopted for the second solution containing $In^{3+}_{(aq)}$ and $NO^-_{3(aq)}$ ions. The pHmeter (QUIMIS®, Brazil) registered pH values of 9.6 and 3.1 for these solutions, respectively. The complete dissolution of their respective chemical precursors [$Na_2WO_4{\cdot}2H_2O$ and $In(NO_3)_3{\cdot}H_2O$] is described in the following equations:

$$3Na_2WO_4 \cdot 2H_2O_{(s)} \xrightarrow{H_2O} 6Na^+_{(aq)} + 3WO^{2-}_{4(aq)} + 6H_2O_{(l)} \quad (1)$$

$$2In(NO_3)_3 \cdot 6H_2O_{(s)} \xrightarrow{H_2O} 2In^{3+}_{(aq)} + 6NO^-_{3(aq)} + 12H_2O_{(l)} \quad (2)$$

This experimental procedure was performed five times. Before mixing the solutions for the formation of amorphous precipitates, we perform a fine pH adjustment in the first solution by means of nitric acid (HNO_3; 70% purity, Meck). The pH values used in this solution were 2; 2.5; 3; 3.5 and 4. Similar the first solution, ammonium hydroxide solution ($NH_3{\cdot}H_2O$; 30% purity, Vetec) and HNO_3 were employed to adjust the pH of the second solution. In this case, $NH_3{\cdot}H_2O$ to acquire pH at 3.5 and 4.0, while the HNO_3 for pH from 2 to 3. Finally, after these pH adjustments, the second solution (100 mL) was mixed with the first solution (100 mL) in a same pH condition. This mixture was maintained under constant stirring at 363 K for 1 h. After this process, the formation of a white suspension with precipitates was verified. This reaction is described by Eq. (3):

$$18H^{+}_{(aq)}+6Na^{+}_{(aq)}+3WO^{2-}_{4(aq)}+6H_2O_{(l)}+2In^{3+}_{(aq)}+6NO^{-}_{3(aq)} +12H_2O_{(l)} \xrightarrow{H_2O(\text{same pH values})} In_2W_3O_{12(s)\text{amorphous}}+6Na^{+}_{(aq)} +6NO^{-}_{3(aq)}+18H_3O^{+}_{(l)} \quad (3)$$

These suspensions containing white precipitates were washed fifteen times (water and acetone), centrifuged (8500 rpm for 10 min), and subsequently dried in a conventional furnace for 338 K for 10 h. Finally, the amorphous precipitates were calcined at 1073 K for 2 h, maintaining a heating rate of 274 K/min (Electronic Supplementary Material with XRD patterns and TGA analysis of both $In_2W_3O_{12}$ and $In_6W_3O_{12}$ powders obtained at pH 4).

Characterizations of $In_2W_3O_{12}$ and $In_6W_3O_{12}$ powders

The structural analysis of all powders was performed by means of XRD patterns by using a LabX XRD-6000 diffractometer (Shimadzu®, Japan) with CuKα radiation ($\lambda = 0.154184$ nm). Data were collected over 2θ ranging from 10° to 40° with a scanning scan rate and step size of 2°/min and 0.02°, respectively. The *PowderCell* software [28] was employed to identify all crystallographic phases. For Rietveld analysis, XRD patterns were acquired by using a D/Max-2500PC diffractometer (Rigaku, Japan) with CuKα radiation. Data were collected over 2θ ranging from 10° to 110° with a scanning scan rate and step size of 0.2°/min and 0.02°, respectively. Ultraviolet–Visible (UV–Vis) spectra were measured on a Cary 5G Spectrophotometer (Varian, USA) operated in diffuse-reflectance mode.

Results and discussion

Structural analysis of $In_2W_3O_{12}$ –$In_6W_3O_{12}$ powders

Figs. 1(a, b) illustrate XRD patterns of all powders synthesized by the co-precipitation with different pH values and heat treated at 1073 K for 2 h.

XRD patterns were employed to identify the crystallographic phases and analyze the degree of crystallization of $In_2W_3O_{12}$ powders. Firstly, two different crystalline phases were identified in XRD patterns for the powders synthesized with pH ranging from 2 to 3.5 (Fig. 1(a)). The majority phase was indexed to $In_2W_3O_{12}$ with a monoclinic structure and space group ($P2_1/a$) ("Inorganic Crystal Structure Data" (ICSD) No. 99607) [5], while the secondary phase was ascribed to the polymorph of γ-WO_3 with monoclinic structure and space group ($P2_1/n$) (ICSD No. 50727) [29]. However, when the pH was adjusted at 4, diffraction peaks related to γ-WO_3 disappeared completely (Fig. 1(b)). Besides the $In_2W_3O_{12}$, the appearing of a new phase indexed to In_6WO_{12} with rhombohedral structure and space group ($R\bar{3}$) was clearly detected in this system (ICSD No. 27197) [7]. In principle, pH values superior to 4 considerably favors the crystallization of In_6WO_{12}. All these XRD patterns confirm that the pH plays a fundamental role for the formation of the desired $In_2W_3O_{12}$ phase. All our results are consistent with the data previously published in the literature [30].

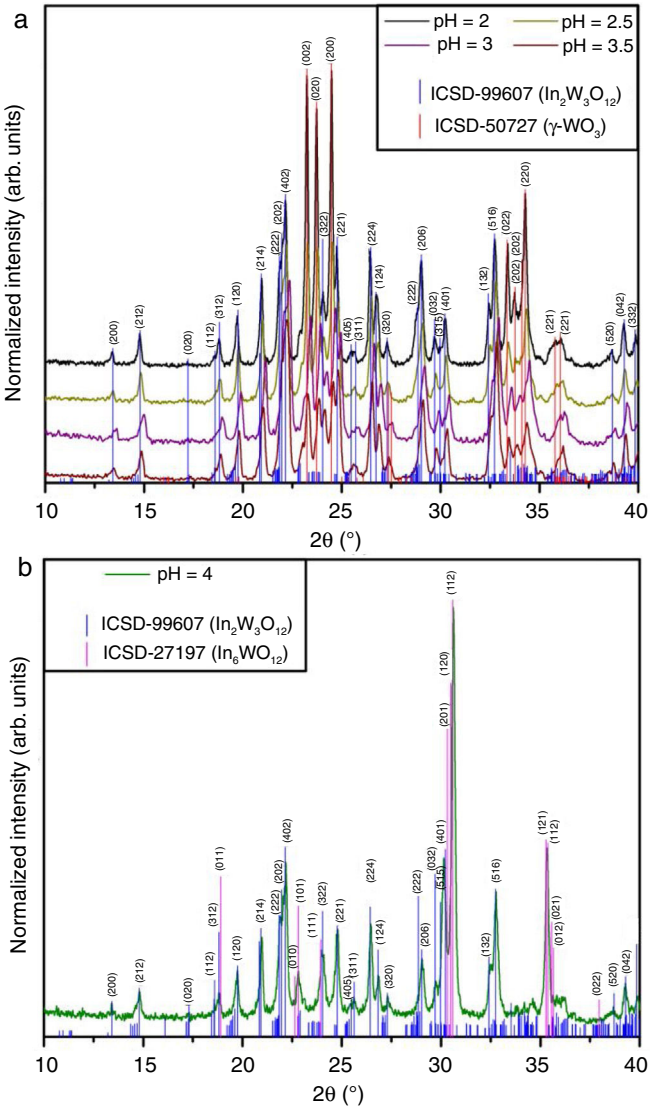

Fig. 1 – XRD patterns of $In_2W_3O_{12}$ and In_6WO_{12} powders obtained with pH ranging from 2 to 3.5 (a) and pH at 4 (b) with posterior heat treatment at 1073 K for 2 h.

Quantitative analysis of $In_2W_3O_{12}$ and $In_6W_3O_{12}$ powders by Rietveld method

The indexing of the phases was conducted by using the structural characterization data obtained from XRD patterns (experimental) with the respective crystallographic files (theoretical) [ICSD No. 99607 ($In_2W_3O_{12}$), 50727 (γ-WO_3), and 27197 (In_6WO_{12})] by using the *ReX.Cell* software [31]. In addition, the general structure analysis software (GSAS) software was used [32] to perform the Rietveld refinement analysis and quantify the crystalline phases in the samples.

The Rietveld refinement method is a least squares refinement procedure wherein the experimental step-scanned values are adapted to the calculated ones. The profiles are considered to be known, and a model for the crystal structure

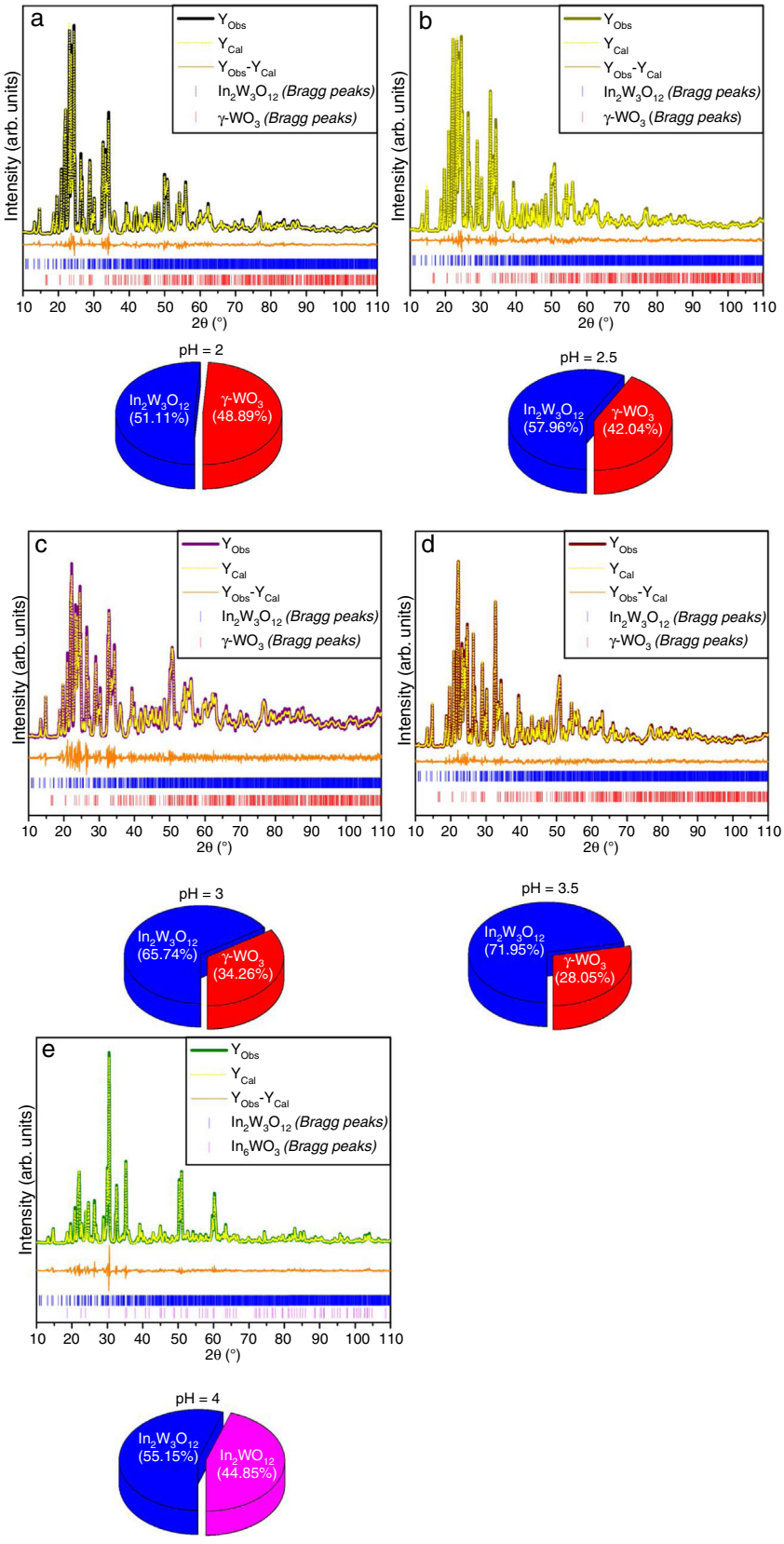

Fig. 2 – Rietveld refinement plot of $In_2W_3O_{12}$–In_6WO_{12} powders synthesized at (a) pH = 2; (b) pH = 2.5; (c) pH = 3; (d) pH = 3.5; and (e) pH = 4 with posterior heat treatment at 1073 K for 2 h. The weight percentage of all crystallographic phases for each sample is shown as pie chart.

is available [33]. This structural refinement method presents several advantages over conventional quantitative analysis methods. As the method uses a whole pattern fitting algorithm, all lines for each phase are explicitly considered, and even severely overlapped lines are usually not a problem. Thus, it is not necessary to decompose patterns into separate Bragg peaks, as is often the case in traditional methods. The use of all reflections in a pattern rather than only the strongest ones minimizes both the uncertainty in the derived weight fractions and the effects of preferred orientation, primary extinction, and nonlinear detection systems [34].

The experimental lattice parameters, unit cell volumes, phase percentage, length of the chemical bonds, and bond angles between (O—In—O) and (O—W—O) in $In_2W_3O_{12}$, γ-WO_3, and In_6WO_{12} powders were obtained and calculated by using the Rietveld refinement method [35,36] with the GSAS software [32]. The structural refinement results of $In_2W_3O_{12}$ powders obtained at different pH values and heat treated at 1073 K for 2 h are showed in Figs. 2(a–e). In addition, below the respective Rietveld refinements are illustrated in the pie charts indicating the weight percentage for each of the phases found in XRD patterns. The Rietveld refinement results are displayed in Tables 1a-1e

(Electronic Supplementary Material with validation of CIF files and structure factors in PLATON).

The Rietveld refinement results exhibited a good agreement between observed XRD patterns and theoretical results, as illustrated in Fig. 2(a–e). As can be seen, the difference between experimentally observed XRD patterns and the theoretically calculated data was close to zero in terms of the scale of intensity, as indicated by the line ($Y_{Observed} - Y_{Calculated}$). In a first observation, for pH ranging from 2 to 3.5 in the aqueous solution, the powders heat treated at 1073 K for 2 h revealed a reduction of γ-WO_3 as well as an increase of $In_2W_3O_{12}$ with the increase of pH value (Figs. 2(a–e)). In contrast, the powders obtained with pH adjusted at 4 showed a mixture of In_6WO_{12} and In_6WO_{12} phases. This information implies in the difficulty of forming the desired pure $In_2W_3O_{12}$ phase.

Based on our experimental data, we propose the following reactions induced by the heat treatment at 1073 K for 2 h:

$$4In_2O_{3(s)amorphous} + 4WO_{3(s)amorphous} \xrightarrow{1073\,K/2\,h} In_6WO_{12(s)} + In_2W_3O_{12(s)} \quad (4)$$

A possible reaction performed pH at 4 is related to the formation of solid In_2O_3 and WO_3 stoichiometric phases (both in amorphous state) when precipitated at 363 K for 1 h (Eq. (4)). More details on the Rietveld refinement analysis are presented in Tables 1a-1e.

In Tables 1a-1e, the statistical parameters (R_p, R_{wp}, R_{Bragg}, χy, and S) exhibited small deviations, which indicate the good quality of the structural refinements. The structural refinement data confirmed that all $In_2W_3O_{12}$ powders were crystallized in a monoclinic structure with space group ($P2_1/a$), point-group symmetry (C_{2h}^5), and eight molecular formula units per unit cell (Z = 8). The secondary or deleterious phase

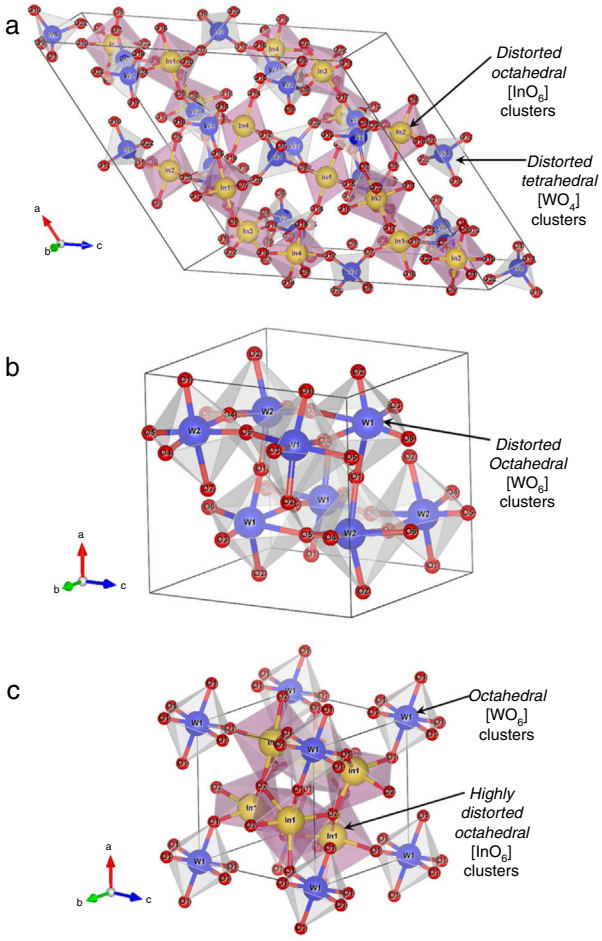

Fig. 3 – Schematic representation of (a) monoclinic $In_2W_3O_{12}$ unit cell, (b) monoclinic γ-WO_3 unit cell, and (c) rhombohedral In_6WO_{12} unit cell, respectively.

was identified as γ-WO_3, which has a monoclinic structure with space group ($P2_1/a$), point-group symmetry (C_{2h}^5), and eight molecular formula units per unit cell (Z = 8). Therefore, these powders are isostructural with a small difference in their space group due to an inversion in the center of symmetry, which leads to changes in (x, y, z) atomic coordinates [37].

The Rietveld refinement data confirmed that the $In_2W_3O_{12}$ powders synthesized at pH = 4 exhibited a deleterious phase related to In_6WO_{12}, which presents a rhombohedral structure with space group ($R\bar{3}$), point-group symmetry (S_6), and one molecular formula unit per unit cell (Z = 1). Moreover, small variations in the atomic positions of In, W, and O atoms were observed because the atoms do not occupy fixed positions in this specific type of structure. These results indicate major variations in the position of O atoms because of distortion caused in the lattice, as demonstrated by the XRD technique. These distortions are able to influence in bond lengths and angles of In—O or W—O bonds, causing the formation of distorted octahedral [InO_6] clusters and tetrahedral [WO_4] clusters in $In_2W_3O_{12}$ structure.

Table 1a – Rietveld refinement results for $In_2W_3O_{12}$ and In_6WO_{12} powders synthesized by the co-precipitation method at (a) pH = 2, (b) pH = 2.5, (c) pH = 3, (d) pH = 3.5 and (e) pH = 4, and heat treated at 1073 K for 2 h.

Atoms	Wyckoff	Site	x	y	z
(a)					
In1	4e	1	0.38100	0.96400	0.31700
In2	4e	1	0.37200	0.45700	0.05100
In3	4e	1	0.37200	0.47300	0.18700
In4	4e	1	0.10700	0.98400	0.41900
W1	4e	1	−0.00800	0.24900	0.48560
W2	4e	1	0.35620	0.11100	0.13040
W3	4e	1	0.14010	0.11300	0.25580
W4	4e	1	0.14900	0.61500	0.38260
W5	4e	1	0.35160	0.63000	0.21690
W6	4e	1	−0.00200	0.74900	0.01840
O1	4e	1	0.58170	0.38720	−0.00010
O2	4e	1	0.98820	0.40750	0.17150
O3	4e	1	0.82800	0.19370	0.09490
O4	4e	1	0.77440	0.49740	0.05440
O5	4e	1	0.52250	0.42530	0.14430
O6	4e	1	0.73210	0.51940	0.27280
O7	4e	1	0.42040	0.10990	0.41390
O8	4e	1	0.18430	0.28540	0.24640
O9	4e	1	0.54820	0.30880	0.44370
O10	4e	1	0.38770	0.30880	0.97530
O11	4e	1	0.06440	0.38180	0.06740
O12	4e	1	0.41150	0.36270	0.50100
O13	4e	1	0.41150	0.38290	0.23250
O14	4e	1	0.24840	0.03960	0.51280
O15	4e	1	0.11640	0.10650	0.33240
O16	4e	1	0.53270	0.94320	0.36260
O17	4e	1	0.74220	0.95970	0.19260
O18	4e	1	0.66540	0.93780	0.30070
O19	4e	1	0.96190	0.93390	0.31160
O20	4e	1	0.09450	0.31110	0.59390
O19	4e	1	0.15680	0.80620	0.39130
O22	4e	1	0.04510	0.65770	0.12100
O23	4e	1	0.36290	0.60270	0.12280
O24	4e	1	0.34380	0.81710	0.22570
W1	4e	1	0.25300	0.02600	0.28300
W2	4e	1	0.24600	0.03300	0.78110
O1	4e	1	0.00000	0.03000	0.21800
O2	4e	1	0.00200	0.46400	0.22100
O3	4e	1	0.28200	0.26400	0.27700
O4	4e	1	0.21400	0.25700	0.74200
O5	4e	1	0.27700	0.02800	0.00020
O6	4e	1	0.28800	0.49800	0.00000

[Phase 1: $In_2W_3O_{12}$; $P2_1/a$ (14) – Monoclinic ($a = 16.3624(8)$ Å, $b = 9.6366(3)$ Å, $c = 19.0316(8)$ Å; $V = 2448.7(2)$ Å^3; $\beta = 125.3149(3)^\circ$, $Z = 8$ and $\rho = 5.27932$ g/cm^3)] and [Phase 2: γ-WO_3; $P2_1/n$ (14) – Monoclinic ($a = 7.3072(2)$ Å, $b = 7.5376(2)$ Å, $c = 7.6961(2)$ Å, $V = 423.86(1)$ Å^3; $\beta = 90.735(4)^\circ$, $Z = 8$ and $\rho = 7.26599$ g/cm^3]; $R_p = 5.88\%$; $R_{wp} = 7.79\%$; $R_{Bragg} = 4.12\%$; $\chi^2 = 2.89$ and $S = 1.70$. Weights of the phases in the $In_2W_3O_{12}$ Monoclinic = 51.11% and γ-WO_3 Monoclinic = 48.89%.

Crystalline structure, symmetry, and coordination clusters of $In_2W_3O_{12}$, γ-WO_3, and In_6WO_{12} lattices

Fig. 3(a–c) illustrates schematic representations of crystalline structures, symmetry, geometry, and coordination of $In_2W_3O_{12}$, γ-WO_3, and In_6WO_{12} powders, respectively.

All these structures were modeled using the visualization system for electronic and structural analysis (VESTA) software (version 3.4.3) [38,39] with the lattice parameters and atomic positions obtained from Rietveld refinement results (Tables 1a-1e) as input data. In $In_2W_3O_{12}$ structure (Fig. 3(a)), In atoms are coordinated to six O atoms, forming distorted octahedral [InO_6] clusters with symmetry group (O_h). These octahedron-type polyhedrons have 6-vertices, 8-faces, and 12-edges [40]. In addition, W atoms are coordinated to four O atoms, forming distorted tetrahedral [WO_4] clusters with symmetry group (T_d). These tetrahedron-type polyhedrons are composed of 4-vertices, 4-faces, and 6-edges [41]. For

Table 1b – aaaa.

Atoms	Wyckoff	Site	x	y	z
In1	4e	1	0.38100	0.96400	0.31700
In2	4e	1	0.37200	0.45700	0.05100
In3	4e	1	0.12000	0.47300	0.18700
In4	4e	1	0.10700	0.98400	0.41900
W1	4e	1	−0.00800	0.24900	0.48560
W2	4e	1	0.35620	0.11100	0.13040
W3	4e	1	0.14010	0.11300	0.25580
W4	4e	1	0.14900	0.61500	0.38260
W5	4e	1	0.35160	0.63000	0.21690
W6	4e	1	−0.00200	0.74900	0.01840
O1	4e	1	0.58170	0.38720	−0.00010
O2	4e	1	0.98820	0.40750	0.17150
O3	4e	1	0.82800	0.19370	0.09490
O4	4e	1	0.77440	0.49740	0.05440
O5	4e	1	0.52250	0.42530	0.14430
O6	4e	1	0.73210	0.51940	0.27280
O7	4e	1	0.42040	0.10990	0.41390
O8	4e	1	0.18430	0.28540	0.24640
O9	4e	1	0.54820	0.35360	0.44370
O10	4e	1	0.38770	0.30880	0.97530
O11	4e	1	0.06440	0.38180	0.06740
O12	4e	1	0.41150	0.36270	0.50100
O13	4e	1	0.85750	0.38290	0.23250
O14	4e	1	0.24840	0.03960	0.51280
O15	4e	1	0.11640	0.10650	0.33240
O16	4e	1	0.53270	0.94320	0.36260
O17	4e	1	0.74220	0.95970	0.19260
O18	4e	1	0.66540	0.93780	0.30070
O19	4e	1	0.96190	0.93390	0.31160
O20	4e	1	0.09450	0.31110	0.59390
O19	4e	1	0.15680	0.80620	0.39130
O22	4e	1	0.04510	0.65770	0.12100
O23	4e	1	0.36290	0.60270	0.12280
O24	4e	1	0.34380	0.81710	0.22570
W1	4e	1	0.25300	0.02600	0.28300
W2	4e	1	0.24600	0.03300	0.78110
O1	4e	1	0.00000	0.03000	0.21800
O2	4e	1	0.00200	0.46400	0.22100
O3	4e	1	0.28200	0.26400	0.27700
O4	4e	1	0.21400	0.25700	0.74200
O5	4e	1	.27700	0.02800	0.00020
O6	4e	1	0.28800	0.49800	0.00000

[Phase 1: $In_2W_3O_{12}$; $P2_1/a$ (14) – Monoclinic ($a = 16.3664(7)$ Å, $b = 9.6372(3)$ Å, $c = 19.0353(7)$ Å; $V = 2449.7(1)$ Å^3; $\beta = 125.3216(25)^\circ$, $Z = 8$ and $\rho = 5.27708$ g/cm^3)] and [Phase 2: γ-WO_3; $P2_1/n$ (14) – Monoclinic ($a = 7.3106(3)$ Å, $b = 7.5343(2)$ Å, $c = 7.6991(2)$ Å, $V = 424.05(2)$ Å^3; $\beta = 90.613(7)^\circ$, $Z = 8$ and $\rho = 7.26282$ g/cm^3]; $R_p = 5.57\%$; $R_{wp} = 7.46\%$; $R_{Bragg} = 4.29\%$; $\chi^2 = 2.22$ and $S = 1.49$. Weights of the phases in the $In_2W_3O_{12}$ Monoclinic = 57.96% and γ-WO_3 Monoclinic = 42.04%.

γ-WO_3 structure (Fig. 3(b)), all W atoms are bonded to six O atoms, resulting in distorted octahedral [WO_6] clusters. The existence of distortion in W—O—W bonds of [WO_6]–[WO_6] clusters can be easily noted in this structure.

Finally, In_6WO_{12} structure has its In atoms coordinated to six O atoms, resulting in distorted octahedral [InO_6] clusters. Moreover, W atoms are coordinated to six O atoms, forming octahedral [WO_6] clusters (Fig. 3(c)). The Jahn–Teller (JT) effects can be actuating on octahedral [InO_6] clusters ($In_2W_3O_{12}$), octahedral [WO_6] clusters (γ-WO_3), and both octahedral [InO_6]/[WO_6] clusters (In_6WO_{12}) [42]. This JT effect is caused by the symmetry breaking in octahedral [InO_6]/[WO_6] clusters, in which the two axial bonds can be shorter or longer than the equatorial bonds. Consequently, this phenomenon reduces the symmetry and energy in the lattice [43]. In principle, $In_2W_3O_{12}$ powders are able to present variations in both (O–In–O)/(O–W–O) bond angles and lengths, causing distortions in octahedral [InO_6] and tetrahedral [WO_4] clusters with distinct degrees of order-disorder in the lattice.

UV–Vis spectra and optical band gap energy analysis of $In_2W_3O_{12}$ and $In_6W_3O_{12}$ powders

The optical band gap energy (E_{gap}) was calculated by using the Kubelka–Munk equation [44], which is based on the transformation of diffuse reflectance measurements to estimate E_{gap}

Table 1c – aaaa.

Atoms	Wyckoff	Site	x	y	z
In1	4e	1	0.38100	0.96400	0.31700
In2	4e	1	0.37200	0.45700	0.05100
In3	4e	1	0.12000	0.47300	0.18700
In4	4e	1	0.10700	0.98400	0.41900
W1	4e	1	−0.00800	0.24900	0.48560
W2	4e	1	0.35620	0.11100	0.13040
W3	4e	1	0.14010	0.11300	0.25580
W4	4e	1	0.14900	0.61500	0.38260
W5	4e	1	0.35160	0.63000	0.21690
W6	4e	1	−0.00200	0.74900	0.01840
O1	4e	1	0.58170	0.38720	−0.00010
O2	4e	1	0.98820	0.40750	0.17150
O3	4e	1	0.82800	0.19370	0.09490
O4	4e	1	0.77440	0.49740	0.05440
O5	4e	1	0.52250	0.42530	0.14430
O6	4e	1	0.73210	0.51940	0.27280
O7	4e	1	0.42040	0.10990	0.41390
O8	4e	1	0.18430	0.28540	0.24640
O9	4e	1	0.54820	0.35360	0.44370
O10	4e	1	0.38770	0.30880	0.97530
O11	4e	1	0.06440	0.38180	0.06740
O12	4e	1	0.41150	0.36270	0.50100
O13	4e	1	0.85750	0.38290	0.23250
O14	4e	1	0.24840	0.03960	0.51280
O15	4e	1	0.11640	0.10650	0.33240
O16	4e	1	0.53270	0.94320	0.36260
O17	4e	1	0.74220	0.95970	0.19260
O18	4e	1	0.66540	0.93780	0.30070
O19	4e	1	0.96190	0.93390	0.31160
O20	4e	1	0.09450	0.31110	0.59390
O19	4e	1	0.15680	0.80620	0.39130
O22	4e	1	0.04510	0.65770	0.12100
O23	4e	1	0.36290	0.60270	0.12280
O24	4e	1	0.34380	0.81710	0.22570
W1	4e	1	0.25300	0.02600	0.28300
W2	4e	1	0.24600	0.03300	0.78110
O1	4e	1	0.00000	0.03000	0.21800
O2	4e	1	0.00200	0.46400	0.22100
O3	4e	1	0.28200	0.26400	0.27700
O4	4e	1	0.21400	0.25700	0.74200
O5	4e	1	0.27700	0.02800	0.00020
O6	4e	1	0.28800	0.49800	0.00000

[Phase 1: $In_2W_3O_{12}$; $P2_1/a$ (14) – Monoclinic ($a = 16.3752(2)$ Å, $b = 9.6415(6)$ Å, $c = 19.0521(2)$ Å; $V = 2454.65(2)$ Å^3; $\beta = 125.309(6)^\circ$, $Z = 8$ and $\rho = 5.26644$ g/cm^3)] and [Phase 2: γ-WO_3; $P2_1/n$ (14) – Monoclinic ($a = 7.3126(6)$ Å, $b = 7.5398(7)$ Å, $c = 7.7023(7)$ Å, $V = 424.65(6)$ Å^3; $\beta = 90.615(15)^\circ$, $Z = 8$ and $\rho = 7.25259$ g/cm^3]; $R_p = 7.60\%$; $R_{wp} = 10.16\%$; $R_{Bragg} = 3.20\%$; $\chi^2 = 1.99$ and $S = 1.41$. Weights of the phases in the $In_2W_3O_{12}$ Monoclinic = 65.74% and γ-WO_3 Monoclinic = 34.26%.

values with good accuracy [45]. The Kubelka–Munk equation for any wavelength is described by the following Eq. (5):

$$F(R_\infty) = \frac{(1 - R_\infty)^2}{2R_\infty} = \frac{k}{s} \quad (5)$$

where $F(R_\infty)$ is the Kubelka–Munk function or the absolute reflectance of the sample. The magnesium oxide was adopted as standard sample in reflectance measurements; $R_\infty = R_{sample}/R_{MgO}$ (R_∞ is the reflectance), k is the molar absorption coefficient, and s is the scattering coefficient. The optical band gap and absorption coefficient of semiconductor oxides [46] can be calculated using Eq. (6):

$$\alpha h\nu = C_1(h\nu - E_{gap})^n \quad (6)$$

where α is the linear absorption coefficient of the material, $h\nu$ is the photon energy, C_1 is a proportionality constant, E_{gap} is the optical band gap, and n is a constant associated to different kinds of electronic transitions ($n = 0.5$ for direct allowed, $n = 2$ for indirect allowed, $n = 1.5$ for direct forbidden, and $n = 3$ for indirect forbidden). According to the literature [47–49], trivalent tungstates, such as $Al_2W_3O_{12}$, $Gd_2W_3O_{12}$, $Y_2W_3O_{12}$ and $In_2W_3O_{12}$ powders, have an optical absorption spectrum

Table 1d – aaaa.

Atoms	Wyckoff	Site	x	y	z
In1	4e	1	0.38100	0.96400	0.31700
In2	4e	1	0.37200	0.45700	0.05100
In3	4e	1	0.12000	0.47300	0.18700
In4	4e	1	0.10700	0.98400	0.41900
W1	4e	1	−0.00800	0.24900	0.48560
W2	4e	1	0.35620	0.11100	0.13040
W3	4e	1	0.14010	0.11300	0.25580
W4	4e	1	0.14900	0.61500	0.38260
W5	4e	1	0.35160	0.63000	0.21690
W6	4e	1	−0.00200	0.74900	0.01840
O1	4e	1	0.58170	0.38720	−0.00010
O2	4e	1	0.98820	0.40750	0.17150
O3	4e	1	0.82800	0.19370	0.09490
O4	4e	1	0.77440	0.49740	0.05440
O5	4e	1	0.52250	0.42530	0.14430
O6	4e	1	0.73210	0.51940	0.27280
O7	4e	1	0.42040	0.10990	0.41390
O8	4e	1	0.18430	0.28540	0.24640
O9	4e	1	0.54820	0.35360	0.44370
O10	4e	1	0.38770	0.30880	0.97530
O11	4e	1	0.06440	0.38180	0.06740
O12	4e	1	0.41150	0.36270	0.50100
O13	4e	1	0.41150	0.38290	0.23250
O14	4e	1	0.24840	0.03960	0.51280
O15	4e	1	0.11640	0.10650	0.33240
O16	4e	1	0.53270	0.94320	0.36260
O17	4e	1	0.74220	0.95970	0.19260
O18	4e	1	0.66540	0.93780	0.30070
O19	4e	1	0.96190	0.93390	0.31160
O20	4e	1	0.09450	0.31110	0.59390
O19	4e	1	0.15680	0.80620	0.39130
O22	4e	1	0.04510	0.65770	0.12100
O23	4e	1	0.36290	0.60270	0.12280
O24	4e	1	0.34380	0.81710	0.22570
W1	4e	1	0.25300	0.02600	0.28300
W2	4e	1	0.24600	0.03300	0.78110
O1	4e	1	0.00000	0.03000	0.21800
O2	4e	1	0.00200	0.46400	0.22100
O3	4e	1	0.28200	0.26400	0.27700
O4	4e	1	0.21400	0.25700	0.74200
O5	4e	1	0.27700	0.02800	0.00020
O6	4e	1	0.28800	0.49800	0.00000

[Phase 1: $In_2W_3O_{12}$; $P2_1/a$ (14) – Monoclinic ($a = 16.3679(6)$ Å, $b = 9.6402(3)$ Å, $c = 19.0454(7)$ Å; $V = 2451.63(9)$ Å^3; $\beta = 125.3327(3)^\circ$, $Z = 8$ and $\rho = 5.27292$ g/cm^3)] and [Phase 2: γ-WO_3; $P2_1/n$ (14) – Monoclinic ($a = 7.30724(2)$, $b = 7.53764(2)$ Å, $c = 7.69613(2)$ Å, $V = 423.863(2)$ Å^3; $\beta = 90.735(4)^\circ$, $Z = 8$ and $\rho = 7.26628$ g/cm^3]; $R_p = 5.46\%$; $R_{wp} = 7.30\%$; $R_{Bragg} = 3.30\%$; $\chi^2 = 1.59$ and $S = 1.26$. Weights of the phases in the $In_2W_3O_{12}$ Monoclinic = 71.95% and γ-WO_3 Monoclinic = 28.05%.

governed by direct or indirect electronic transitions. In direct electronic transitions, after the electronic absorption process, electrons located in the minimum energy states in the conduction band (CB) return to maximum energy states of the valence band (VB) at the same points in the Brillouin zone [50]. On the other hand, for indirect electronic transitions, the electronic process occurs at distinct points in the Brillouin zone [51]. Based on this information and literature [52], E_{gap} values of $In_2W_3O_{12}$ powders were calculated with $n = 0.5$ in Eq. (6). Finally, by using the absolute reflectance function in Eq. (5) with $k = 2\alpha$, the modified Kubelka–Munk equation is described as in Eq. (7):

$$[F(R_\infty)h\nu]^2 = C_2(h\nu - E_{gap}) \quad (7)$$

Therefore, by determining the value of $F(R_\infty)$ from Eq. (7) and plotting a graph of $[F(R_\infty)h\nu]^2$ against $h\nu$, E_{gap} values were calculated for all powders by extrapolating the linear portion of UV–Vis curves.

Figs. 4(a–e) illustrate the UV–Vis spectra of all powders obtained at different pH values and heat-treated at 1073 K for 2 h. The evolution of E_{gap} as a function of different pH values is illustrated in Fig. 4(f). Insets show the digital photos of each powder.

An important point to be considered is that there is a slight increase of E_{gap} values with the increase of pH condition for the powders heat treated at 1073 K for 2 h. This behavior is caused by the reduction of intermediary energy levels between the VB and CB. The origin these intermediary energy levels

Table 1e – aaaa.

Atoms	Wyckoff	Site	x	y	z
In1	4*e*	1	0.38100	0.96400	0.31700
In2	4*e*	1	0.37200	0.45700	0.05100
In3	4*e*	1	0.12000	0.47300	0.18700
In4	4*e*	1	0.10700	0.98400	0.41900
W1	4*e*	1	−0.00800	0.24900	0.48560
W2	4*e*	1	0.35620	0.11100	0.13040
W3	4*e*	1	0.14010	0.11300	0.25580
W4	4*e*	1	0.14900	0.61500	0.38260
W5	4*e*	1	0.35160	0.63000	0.21690
W6	4*e*	1	−0.00200	0.74900	0.01840
O1	4*e*	1	0.58170	0.38720	−0.00010
O2	4*e*	1	0.98820	0.40750	0.17150
O3	4*e*	1	0.82800	0.19370	0.09490
O4	4*e*	1	0.77440	0.49740	0.05440
O5	4*e*	1	0.52250	0.42530	0.14430
O6	4*e*	1	0.73210	0.51940	0.27280
O7	4*e*	1	0.42040	0.10990	0.41390
O8	4*e*	1	0.18430	0.28540	0.24640
O9	4*e*	1	0.54820	0.35360	0.44370
O10	4*e*	1	0.38770	0.30880	0.97530
O11	4*e*	1	0.06440	0.38180	0.06740
O12	4*e*	1	0.41150	0.36270	0.50100
O13	4*e*	1	0.41150	0.38290	0.23250
O14	4*e*	1	0.24840	0.03960	0.51280
O15	4*e*	1	0.11640	0.10650	0.33240
O16	4*e*	1	0.53270	0.94320	0.36260
O17	4*e*	1	0.74220	0.95970	0.19260
O18	4*e*	1	0.66540	0.93780	0.30070
O19	4*e*	1	0.96190	0.93390	0.31160
O20	4*e*	1	0.09450	0.31110	0.59390
O19	4*e*	1	0.15680	0.80620	0.39130
O22	4*e*	1	0.04510	0.65770	0.12100
O23	4*e*	1	0.36290	0.60270	0.12280
O24	4*e*	1	0.34380	0.81710	0.22570
In1	3*a*	1	0.13970	0.32140	0.60440
W1	18*f*	1	0	0	0
O1	18*f*	1	−0.04260	0.09740	0.29690
O2	18*f*	1	0.40570	0.58380	0.82190

[Phase 1: $In_2W_3O_{12}$; $P2_1/a$ (14) – Monoclinic ($a = 16.3757(11)$ Å, $b = 9.6365(4)$ Å, $c = 19.0385(1)$ Å; $V = 2450.56(2)$ Å^3; $\beta = 125.3465(3)^\circ$, $Z = 8$ and $\rho = 5.27522$ g/cm^3)] and [Phase 2: In_6WO_{12}; $R\bar{3}$ (148) – Trigonal ($a = b = 6.2344(1)$ Å, $c = 6.2344$ Å, $V = 232.19(1)$ Å^3; $Z = 1$ and $\rho = 7.61446$ g/cm^3]; $R_p = 8.22\%$; $R_{wp} = 10.93\%$; $R_{Bragg} = 4.70\%$; $\chi^2 = 3.80$ and $S = 1.95$. Weights of the phases in the $In_2W_3O_{12}$ Monoclinic = 55.15% and In_6WO_{12} Trigonal = 44.85%.

Table 2 – Comparative results between E_{gap} values of $In_2W_3O_{12}$–In_6WO_{12} powders obtained in this study with those reported in the literature.

Method	Material	Shape	Temperature (K)	Time (h)	E_{gap} (eV)	Ref.
Sol–gel	In_6WO_{12}	Thin film	873	1	4.1	[16]
Sol–gel	In_6WO_{12}	Thin film	973	1	3.8	[16]
Solid state reaction	In_6WO_{12}	Ceramics	1473	12	3.3	[27]
PWPPTEC	In_6WO_{12}	Crystal	–	–	2.0	[27]
–	$In_2W_3O_{12}$	–	–	–	–	d
CP	$In_2W_3O_{12}$–γ-WO_3	Powder	1073	2	2.88	✠
CP	$In_2W_3O_{12}$–γ-WO_3	Powder	1073	2	2.92	✠
CP	$In_2W_3O_{12}$–γ-WO_3	Powder	1073	2	2.95	✠
CP	$In_2W_3O_{12}$–γ-WO_3	Powder	1073	2	2.90	✠
CP	$In_2W_3O_{12}$–In_6WO_{12}	Powder	1073	2	3.73	✠

SG = Sol–Gel; SSR = Solid state reaction; PWPPTEC = Plane-Wave Pseudo-Potential Total Energy Calculation; CP = Co-Precipitation; E_{gap} = optical band gap energy; Ref. = reference; d = Not yet reported in the literature and ✠ = this work.

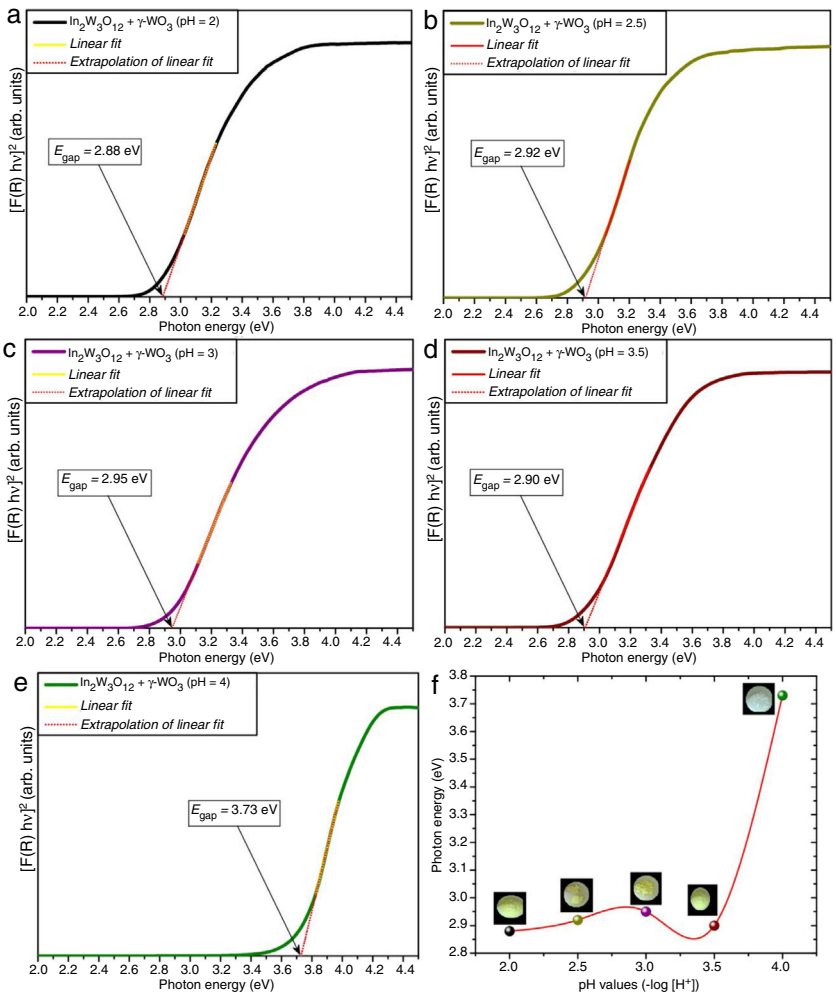

Fig. 4 – UV–Vis spectra of $In_2W_3O_{12}$–In_6WO_{12} powders synthesized at (a) pH = 2, (b) pH = 2.5, (c) pH = 3, (d) pH = 3.5, and (e) pH = 4, (f) evolution of E_{gap} values as a function of different pH values. Insets show the digital photos of each powder.

is due to defects arising from modifications in bond lengths and/or distortions in bond angles between O-In_O ([InO_6] clusters) or O-W-O bonds ([WO_6] clusters), respectively [53]. As identified in Rietveld refinement results (Tables 1a-1d), the increase of pH from 2 to 3.5 promoted a reduction of secondary phase (γ-WO_3) in $In_2W_3O_{12}$ powders. Therefore, there is a decreasing and reorganization of intermediary energy levels in the band gap arising from γ-WO_3, causing an increase of E_{gap} for $In_2W_3O_{12}$ powders Fig. 4(a–d). The literature has reported [54,55] E_{gap} values for γ-WO_3 phase in the range from 2.6 to 2.8 eV [16], while for In_6WO_{12} phase an E_{gap} values of approximately 3.3 eV [27] as illustrated in Fig. 4(e, f). This large difference between the E_{gap} values of the $In_2W_3O_{12}$–WO_3 phases and $In_2W_3O_{12}$–In_6WO_{12} phases illustrated in Fig. 4(d, e) suggest that the In_6WO_{12} phase with the rhombohedral structure has a high energy value between the valence band and conduction band with respect to $In_2W_3O_{12}$ phase with the monoclinic structure, as presented in Table 2.

The results presented in this table indicate a highest E_{gap} value (3.73 eV) can be attributed to the synergic effect of intermediary energy levels arising from both $In_2W_3O_{12}$ and In_6WO_{12} phases (Fig. 4(e, f)). The E_{gap} values obtained in our study are in good agreement with those previously published in the literature [16,27]. Therefore, we propose that this behavior is promoted owing to the simultaneous presence of these $In_2W_3O_{12}$ and In_6WO_{12} complex phases and a change in the color of the powder from the light-green present in this phase mixture ($In_2W_3O_{12}$ and γ-WO_3) to white (inset Fig. 4(f)), which demonstrates a high reflectance and promotes a significant increase in the E_{gap} values.

Conclusions

In summary, $In_2W_3O_{12}$–In_6WO_{12} powders were synthesized by the co-precipitation method at 363 K for 1 h with different pH values (from 2 to 4) and heat treated at 1073 K for 2 h. The pH pre-adjustment was not able to produce phase-pure $In_2W_3O_{12}$ powders. According to XRD patterns and Rietveld refinement result, $In_2W_3O_{12}$ powders formed with pH ranging from 2 to 3.5 exhibited the existence of secondary phase related to γ-WO_3 powders. On the other hand, the synthesis performed with pH at 4 resulted in crystalline powders composed of a mixture of $In_2W_3O_{12}$ and In_6WO_{12} phases. In our systematic study,

the results suggest that employing the methodology with pH pre-adjustment to obtain the monophasic $In_2W_3O_{12}$ powder is possibly found between (pH 3.5 and 4.0). The modifications in bond lengths and/or distortions in bond angles of octahedral [InO_6] clusters ($In_2W_3O_{12}$), octahedral [WO_6] clusters (γ-WO_3), and both octahedral [InO_6]/[WO_6] clusters (In_6WO_{12}) was identified by Rietveld refinement. A slight rise of E_{gap} values were identified with the increase of pH condition for the powders heat treated at 1073 K for 2 h. This phenomenon was related to decreasing and reorganization of intermediary energy levels in the band gap, as a consequence of the reduction of γ-WO_3 in $In_2W_3O_{12}$ powders (pH ranging from 2 to 3.5). The combination of intermediary energy levels arising from $In_2W_3O_{12}$ and In_6WO_{12} phases resulted in the highest E_{gap} (at around 3.73 eV).

Acknowledgements

The authors acknowledge the financial support of the Brazilian research financing institutions: CNPq (479644/2012-8 and 304531/2013-8), FAPESP (2012/14004-5 and 2013/07296-2), and CAPES-PNPD (1268069).

Appendix A. Supplementary data

Supplementary data associated with this article can be found, in the online version, at doi:10.1016/j.bsecv.2019.02.001.

REFERENCES

[1] T.P. Yadav, R.M. Yadav, D.P. Singh, Nanosci. Nanotechnol. 2 (2012) 22–48.
[2] C.C. Koch, Rev. Adv. Mater. Sci. 5 (2003) 91–99.
[3] E.J. Gonzalez, G.J. Piermarini, Handbook of nanostructured materials and nanotechnology, in: Low-temperature Compaction of Nanosize Powders, vol. 1, 2000, pp. 215–249 (Cap. 4).
[4] M. Wilson, K. Kannangara, G. Smith, M. Simmons, B. Raguse, Nanotechnology: Basic Science and Emerging Technologies, vol. 2, CRC Press Company, Boca Raton London, New York, Washington D.C., 2004, pp. 1–264.
[5] A.P. Richards, D.D. Edwards, J. Solid State Chem. 177 (2004) 2740–2748.
[6] A.Y. Neiman, A.V. Karapetyan, N.N. Pestereva, Russ. J. Electrochem. 50 (2014) 58–69.
[7] D. Michel, A. Kahn, Acta Cryst. B 38 (1982) 1437–1441.
[8] V. Sivasubramanian, T.R. Ravindran, R. Nithya, A.K. Arora, J. Appl. Phys. 96 (2004) 387–392.
[9] H. Liu, Z. Zhang, J. Ma, Z. Jun, X. Zeng, Ceram. Internat. 41 (2015) 9873–9877.
[10] J. Köhler, N. Imanaka, G.-Y. Adachi, Z. Anorg, Allg. Chem. 625 (1999) 1890–1896.
[11] V.A. Logacheva, G.S. Grigoryan, A.M. Solodukha, D.A. Khoviv, M.V. Marchukov, A.M. Khoviv, Inorg. Mater. 44 (2008) 311–315.
[12] Y.S. Cho, H.D. Glicksman, V.R.W. Amarakoon, Ceramic Nanopowders, pp. 727–743 in Volume 1 of Nalwa H.S. (ed.): Encyclopedia of Nanoscience and Nanotechnology. American Scientific Publishers, Valencia 2004.
[13] A. Dowling, et al., Nanosci. Nanotechnol. July (2004).
[14] G.M. Whitesides, Small 1 (2005) 172–179.
[15] I. Koseva, A. Yordanova, P. Tzvetkov, V. Nikolov, D. Nihtianova, Mater. Chem. Phys. 132 (2012) 808–814.
[16] W.S. Dabney, N.E. Antolino, B.S. Luisi, A.P. Richard, D.D. Edwards, Thin Solid Films 411 (2002) 192–197.
[17] T.I. Baiz, C.P. Heinrich, N.A. Banek, B.L. Vivekens, C. Lind, J. Solid State Chem. 187 (2012) 195–199.
[18] R.F. Shimanouchi, T. Tsuji, R. Yagi, Y. Matsumoto, H. Nishizawa, IOP Conf. Ser.: Mater. Sci. Eng. 18 (2011) 032025–032028.
[19] A.S. Yordanova, R.S. Iordanova, V.S. Nikolov, I.I. Koseva, P.T. Tzvetkov, Bulg. Chem. Commun. 49 (2017) 91–97.
[20] T.A. Mary, A.W. Sleight, J. Mater. Res. 14 (1999) 912–915.
[21] J.S.O. Evans, T.A. Mary, A.W. Sleight, J. Solid State Chem. 133 (1997) 580–583.
[22] A.E. Borisevich, M.V. Korzhik, G.Y. Drobychev, J.-F. Cavaigna, R. Chipaux, Nuclear Instrum. Methods Phys. Res. A 537 (2005) 228–231.
[23] T. Gaewdang, J.P. Chaminade, A. Garcia, C. Fouassier, M. Pouchard, P. Hagenmuller, Mater. Lett. 18 (1993) 64–68.
[24] A.Y. Neiman, T.E. Kulikova, Russ. J. Electrochem. 43 (2007) 682–693.
[25] T. Kulikova, A. Neiman, A. Kartavtseva, D. Edwards, S. Adams, Solid State Ionics 178 (2008) 1714–1718.
[26] Y. Kobayashi, S. Tamura, N. Imanaka, G. Adachi, Solid State Ionics 113–115 (1998) 545–552.
[27] H. Zhang, X. Chen, Z. Li, L. Liu, T. Yu, Z. Zou, J. Phys. Condens. Matter 19 (2007) 376213–3762118.
[28] W. Kraus, G. Nolze, PowderCell software for Windows, version 2.4, BAM, Berlin, 2000.
[29] T. Vogt, P.M. Woodward, B.A. Hunter, J. Solid State Chem. 144 (1999) 206–2015.
[30] A.Y. Neiman, E.V. Kartseva, N.N. Pestereva, L.M. Fedorova, Russ. J. Phys. Chem. A 85 (2011) 1885–1890.
[31] M. Bortolotti, I. Lonardelli, J. Appl. Cryst. 46 (2013) 259–261.
[32] A.C. Larson, R.B. Von Dreele, General Structure Analysis System (GSAS), Los Alamos National Laboratory Report LAUR, 1994, pp. 86–748.
[33] N. Sahu, S. Panigrahi, Bull. Mater. Sci. 34 (2011) 1495–1500.
[34] V. Esteve, L.E. Ochando, M.M. Reventós, G. Peris, J.M. Amigó, Cryst. Res. Technol. 35 (2000) 1183–1192.
[35] H.M. Rietveld, J. Appl. Crystallogr. 2 (1969) 65–71.
[36] H.M. Rietveld, Acta Crystallogr. 22 (1967) 151–152.
[37] R.J.D. Tilley, Crystals and Crystal Structures, vol. 1, John Wiley & Sons, 2006, pp. 1–272.
[38] K. Momma, F. Izumi, J. Appl. Crystallogr. 41 (2011) 653–658.
[39] K. Momma, F. Izumi, J. Appl. Crystallogr. 44 (2011) 1272–1276.
[40] L.S. Cavalcante, M.A.P. Almeida, W. Avansi Jr., R.L. Tranquilin, E. Long, N.C. Batista, V.R. Mastelaro, M. Siu Li, Inorg. Chem. 51 (2012) 10675–10687.
[41] L.S. Cavalcante, F.M.C. Batista, M.A.P. Almeida, A.C. Rabelo, I.C. Nogueira, N.C. Batista, J.A. Varela, M.R.M.C. Santos, E. Longo, M. Siu Li, RSC Adv. 2 (2012) 6438–6454.
[42] M.A.P. Almeida, L.S. Cavalcante, C. Morilla-Santos, A. Beltrán, J. Andrés, L. Gracia, E. Longo, Mater. Charact. 73 (2012) 124–129.
[43] E.L.S. Souza, J.C. Sczancoski, I.C. Nogueira, M.A.P. Almeida, M.O. Orlandi, M.S. Li, R.A.S. Luz, M.G.R. Filho, E. Longo, L.S. Cavalcante, Ultrason. Sonochem. 38 (2017) 256–270.
[44] P. Kubelka, F. Munk, Z. Fur Tech. Phys. 12 (1931) 593–601.
[45] M.L. Myrick, M.N. Simcock, M. Baranowski, H. Brooke, S.L. Morgan, J.N. Mccutcheon, Appl. Spectrosc. Rev. 46 (2011) 140–165.
[46] R.A. Smith, Semiconductors, 2nd ed., Cambridge University Press, London, 1978, pp. 434.

[47] F.M.C. Batista, F.A. La Porta, L. Gracia, E. Cerdeiras, L. Mestres, M. Siu Li, N.C. Batista, J. Andrés, E. Longo, L.S. Cavalcante, J. Mol. Struct. 1081 (2015) 381–388.
[48] F.B. Bacha, S.M. Borchani, M. Dammak, M. Megdiche, J. Alloys Compd. 712 (2017) 657–665.
[49] X.F. Shi, J.G. Li, Q. Zhu, X.D. Li, X.D. Sun, J. Alloys Compd. 712 (2017) 657–665.
[50] R.A. Roca, J.C. Sczancoski, I.C. Nogueira, M.T. Fabbro, H.C. Alves, L. Gracia, L.P.S. Santos, C.P. de Sousa, J. Andrés, G.E. Luz Jr., E. Longo, L.S. Cavalcante, Catal. Sci. Technol. 8 (2015) 4091–4107.
[51] F.S. Cunha, J.C. Sczancoski, I.C. Nogueira, V.G. de Oliveira, S.M.C. Lustosa, E. Longo, L.S. Cavalcante, CrystEngComm 17 (2015) 8207–8211.
[52] J.W. Tang, Z.G. Zou, J.H. Ye, J. Phys. Chem. B 107 (2003) 14265–14269.
[53] A.F. Gouveia, J.C. Sczancoski, M.M. Ferrer, A.S. Lima, M.R.M.C. Santos, M. Siu Li, R.S. Santos, E. Longo, L.S. Cavalcante, Inorg. Chem. 53 (2014) 5589–5599.
[54] J. Zhu, M. Vasilopoulou, D. Davazoglou, S. Kennou, A. Chroneos, U. Schwingenschlögl, Sci. Rep. 7 (2017) 40882–40890.
[55] E. Albanese, C.D. Valentin, G. Pacchioni, ACS Appl. Mater. Interfaces 9 (2017) 23212–23221.